ACS OMEGA

Article

Cite This: ACS Omega 2018, 3, 11290−11299

http://pubs.acs.org/journal/acsodf

Insight into Sulfur Confined in Ultramicroporous Carbon

M. Helen,*[,†] Thomas Diemant,[‡] Stefan Schindler,[†] R. Jürgen Behm,[†,‡] Michael Danzer,[†,⊥] Ute Kaiser,[§] Maximilian Fichtner,[†,∥] and M. Anji Reddy*[,†]

[†]Helmholtz Institute Ulm (HIU) Electrochemical Energy Storage, Helmholtzstraße 11, D-89081 Ulm, Germany

[‡]Institute of Surface Chemistry and Catalysis, Ulm University, Albert-Einstein-Allee 47, D-89081 Ulm, Germany

[§]Electron Microscopy Group of Materials Science, Central Facility for Electron Microscopy, Ulm University, Albert-Einstein-Allee 11, D-89081 Ulm, Germany

[∥]Institute of Nanotechnology, Karlsruhe Institute of Technology, P.O. Box 3640, D-76021 Karlsruhe, Germany

[⊥]Zentrum für Sonnenenergie- und Wasserstoff-Forschung Baden-Württemberg (ZSW), Lise-Meitner-Straße 24, D-89081 Ulm, Germany

ABSTRACT: Here, we provide a deeper insight into the state of sulfur confined in ultramicroporous carbon (UMC) and clarify its electrochemical reaction mechanism with lithium by corroborating the results obtained using various experimental techniques, such as X-ray photoelectron spectroscopy, electron energy loss spectroscopy, *in situ* Raman spectroscopy, and *in situ* electrochemical impedance spectroscopy. In combination, these results indicate that sulfur in UMC exists as linear polymeric sulfur rather than smaller allotropes. The electrochemical reactivity of lithium with sulfur confined in UMC (pore size ≤0.7 nm) is different from that of sulfur confined in microporous carbon (≤2 nm, or ultramicroporous carbon containing significant amount of micropores) and mesoporous carbon (>2 nm). The observed quasi-solid-state reaction of lithium with sulfur in UMC with a single voltage plateau during the discharge/charge process is due to the effective separation of solvent molecules from the active material. The size of carbon pores plays a vital role in determining the reaction path of lithium with sulfur confined in UMC.

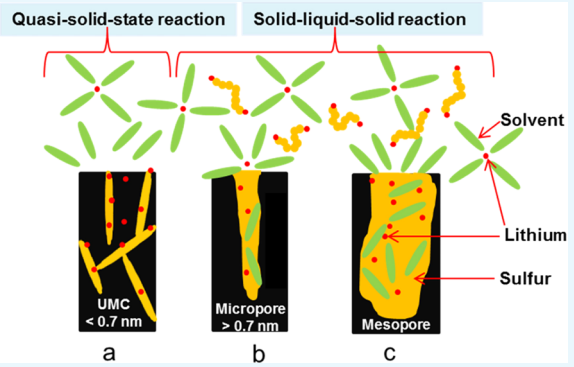

INTRODUCTION

Lithium−sulfur (Li−S) batteries have been the most researched electrochemical energy-storage system recently. Sulfur is an attractive positive electrode material for lithium batteries, mainly due to its high specific capacity (1675 mAh g^{-1}), high specific energy (2600 Wh kg^{-1}), and low cost.[1−3] On the downside, sulfur and its discharge product (Li_2S) are electrical insulators,[4,5] and the lithiation of sulfur results in a large volume change (80%).[6] The reaction of lithium with sulfur in nonaqueous electrolytes (ether-based) results in the formation of lithium polysulfides (Li_xS_8), which are soluble in electrolyte.[7] The dissolved polysulfides diffuse to the anode and get reduced at the anode. The solubility of polysulfide gradually reduces the amount of sulfur in the cathode, thereby limiting the cycle life of Li−S batteries.[8,9] Several strategies have been proposed to overcome these issues related to Li−S batteries, such as (i) by combining sulfur with various conducting matrices like carbon nanotubes (CNTs),[10,11] graphene,[12] porous carbons,[2,13−16] conductive polymers,[17] and metal oxides;[18−20] (ii) by modifying the electrolyte compositions[21] or by opting to ionic liquid electrolytes,[22,23] polymer electrolytes, or solid-state electrolytes;[24,25] and (iii) by modifying the cell configuration.[26,27]

Ultramicroporous carbon (UMC) exhibits unique advantages for the development of sustainable Li−S batteries and other applications.[16,28,29] Since first reports, it has been speculated that UMC confines smaller allotropes of sulfur, thereby eliminating the formation of higher-order lithium polysulfides. Due to space constraints in UMC, the direct contact between sulfur and organic liquid electrolyte solvents is prevented, thereby eliminating the dissolution of active species. This allows the use of carbonate-based solvents in Li−S batteries, which are otherwise considered unsuitable. Despite these advantages, little is known about the state of sulfur confined in UMC and its reactivity toward lithium. Few reports investigated Li reactivity toward sulfur confined in UMC.[7,16,30−32] In our earlier report, we have attempted to investigate the state of sulfur in UMC by transmission electron microscopy (TEM), electron energy loss spectroscopy (EELS), and X-ray photoelectron spectroscopy (XPS) techniques.[16] From XPS analysis, direct transformation of sulfur to lower-order polysulfide Li_2S_2/Li_2S was concluded.[16] However, XPS technique is limited to the surface or subsurface region. Hence,

Received: July 17, 2018
Accepted: August 28, 2018
Published: September 17, 2018

DOI: 10.1021/acsomega.8b01681
ACS Omega 2018, 3, 11290−11299

the state of sulfur confined in UMC and its reactivity toward Li are still unclear. Combining the results obtained using various experimental techniques, such as XPS, EELS, *in situ* Raman spectroscopy, and *in situ* electrochemical impedance spectroscopy (EIS), we here aim at a detailed understanding of the state of sulfur in UMC and its reaction mechanism with Li in carbonate-based electrolytes.

RESULTS AND DISCUSSION

Structure and Morphology of UMC and UMC−S Composite. The UMC−S composite was prepared by the melt-infusion method under vacuum. The synthesis of the UMC host was detailed in our earlier report.[16] UMC and sulfur were mixed at a 1:1 weight ratio, heated at 155 ± 1 °C for 12 h, and cooled to room temperature (RT) under vacuum in a glass oven. Figure 1 shows the N_2 adsorption−desorption

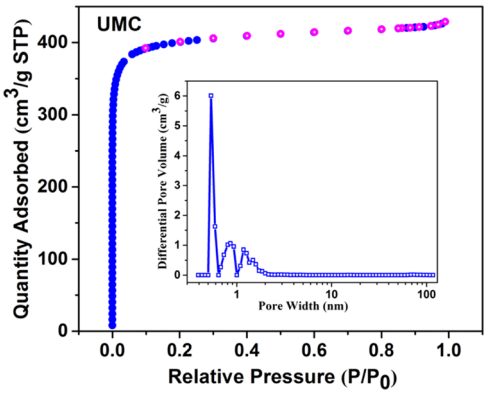

Figure 1. Nitrogen adsorption−desorption isotherm and pore-size distribution (inset) of UMC.

isotherm and pore-size distribution (inset) of the UMC host. The N_2 adsorption−desorption isotherms of UMC exhibit type I isotherm. The Brunauer−Emmett−Teller (BET) surface area and pore volume are 1600 m^2 g^{-1} and 0.66 cm^3 g^{-1}, respectively. The density functional theory (DFT) pore-size distribution curve shows exclusively micropores, most of them with a diameter of 0.53 nm. Figure 2a shows XPS spectra recorded in the S 2p region on a UMC−S composite before sputtering and after 3 and 10 min sputtering. After sputtering, the S−O peak on the surface disappeared and a small peak at a lower binding energy (BE) (162.1 eV) appeared, which was attributed to the C−S interaction.[16] Figure 2b presents the Raman spectra of sulfur, UMC, and UMC−S composite. The Raman spectrum of elemental sulfur has three prominent peaks at 153, 218, and 473 cm^{-1}, which correspond to crystalline sulfur.[33] Raman spectra of UMC and UMC−S composite exhibited only two peaks at around 1330 and 1590 cm^{-1}, which are the characteristic D-band and G-band of carbonaceous materials,[34] respectively. No peaks were detected below 500 cm^{-1} in the case of UMC−S composite due to the lack of sulfur on the surface and to the absorption of any wavelength by the black host material.

The TEM images of UMC and UMC−S composite (Figure 2c) reveal a disordered structure in either case. The energy-filtered TEM analysis of the UMC−S composite showed no sulfur segregates on the surface. Furthermore, EELS measurements were performed to get more insight into the structural and electronic properties of the UMC−S composite. Power-law background-subtracted EELS spectra of the samples are shown in Figure 2d (UMC) and Figure 2e,f (UMC−S composite). The carbon K-edge spectra of UMC and UMC−S (Figure 2d,e) exhibit two main features: (i) a sharp peak at 285 eV corresponding to the 1s → π^* and (ii) a broad feature at >292 eV, corresponding to the 1s → σ^* transitions. The π^* and σ^* peaks at the C-K edge of the UMC−S composite (Figure 2e) are significantly sharpened compared to UMC (Figure 2d). The increased sharpness of the π^* peak reflects an increase in sp^2 hybridization (graphitization) after sulfur incorporation, and the σ^* peak increment indicates an additional contribution due to C−S interactions, which supports the results from XPS. The peaks at 165.7 and 228.7 eV corresponding to the S $L_{2,3}$ edge and S L_1 edge confirm the presence of sulfur in the UMC−S composite (Figure 2f).

State of Sulfur in UMC−S. Figure 3 shows the proposed synthesis scheme for the infusion of sulfur into the UMC host material. During heating, sulfur undergoes various changes. Initially, the room-temperature-stable orthorhombic S_8 converts to monoclinic sulfur (β-S) at 95.5 °C. On further heating to 119 °C, monoclinic sulfur melts, and at above 150 °C, cyclo-S_8 undergoes thermal scission and simultaneously radical polymerization, producing linear, polymeric sulfur chains.[35] Since the glass oven temperature was maintained at 155 °C under reduced pressure, we hypothesize that linear sulfur chains are infused into ultramicropores, driven by capillary forces. The infused linear polymeric sulfur chains tend to align the carbon lattice (graphitization) along the length of the carbon pore. In fact, this conclusion is supported by EELS. EELS spectra of the UMC−S composite recorded at the C-K edge exhibited an increase in π^* peak intensity, indicating ordering (graphitization) after sulfur incorporation. Due to size constraints, the infused linear polymeric sulfur maintains its linear form inside UMC even at RT. The operando X-ray absorption spectroscopy (XAS) measurements of UMC−S electrodes showed the formation of higher-order polysulfide (Li_2S_x) at the very start of discharge.[37] This also indicates that sulfur exists as a linear polymeric chain in UMC and not as smaller allotropes. Sulfur is known to exist as linear chains inside single-walled carbon nanotubes with an inner diameter of 1.1 nm and double-walled carbon nanotubes with an inner diameter of 0.6 nm.[37] It is interesting to note that, although sulfur was infused at 600 °C under vacuum (<1 Pa) into the CNTs, it preferred to exist in linear form at room temperature[37] (sulfur exists as short chains at 600 °C[35]). From the data of the different methods, we conclude that sulfur, in fact, exists as a linear polymeric chain inside UMC, which has pores predominantly with a diameter of 0.5 nm.

Electrochemical Performance of UMC−S in Carbonate and Ether Electrolytes. Figure 4a shows the discharge/charge voltage profiles of the UMC−S composite cathode with carbonate electrolyte (1.0 M $LiPF_6$ in ethylene carbonate (EC)/dimethyl carbonate (DMC) (1:1 v/v)) cycled at C/20. The first discharge curve consists of two plateaus. The short plateau at 2.38 V (vs Li^+/Li) is due to the reaction of lithium with the surface functional groups of the carbon host in the composite electrode (it disappeared after the first cycle). Figure 4b shows the first discharge voltage profile for the as-synthesized carbon host (UMC) with no sulfur infiltrated. A similar plateau at 2.38 V (vs Li^+/Li) is observed in the UMC host due to the reaction of Li with surface functional groups of carbon, which confirms that the plateau observed at 2.38 V corresponds to the reaction of lithium with the carbon host, as it is very similar in the first 100 mAh g^{-1} discharge capacity.

DOI: 10.1021/acsomega.8b01681
ACS Omega 2018, 3, 11290−11299

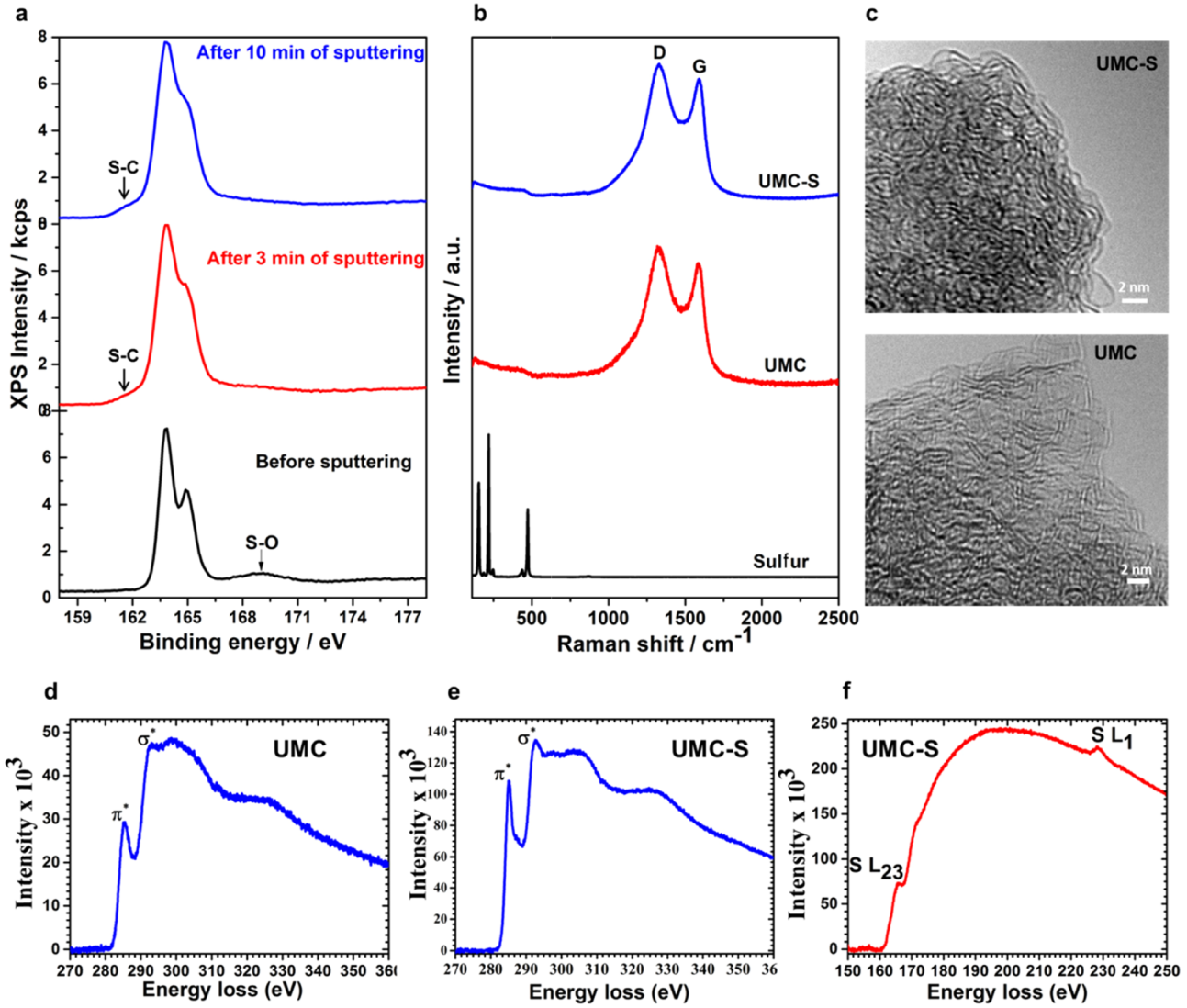

Figure 2. (a) XPS spectra of UMC−S recorded before sputtering and after 3 and 10 min sputtering. (b) Raman spectra of UMC−S of the UMC host material and elemental sulfur. (c) TEM images and (d−f) power-law background-subtracted EELS spectra of UMC and UMC−S composite.

The second discharge plateau at 1.8 V corresponds to the reaction of sulfur in UMC host with Li. Further cycling of the UMC−S composite cathode resulted in a single discharge and charge plateau at 1.8 and 2.2 V (vs Li^+/Li), respectively. A more detailed discussion of the electrochemical characterization results of the UMC−S composite with a carbonate electrolyte was given in our previous report.[16]

The UMC−S cathode with carbonate electrolyte exhibited a large irreversible capacity loss (ICL) in the first cycle (Figure 4a), which could be due to the reaction of polysulfides expelled to the surface. During the discharge process, sulfur is converted to polysulfides, which results in volume changes. Due to this, a fraction of polysulfide might have been expelled to the surface, which reacts irreversibly with carbonate molecules and reduces the amount of sulfur available for the second cycle. Therefore, a possible way to reduce the ICL in the first cycle would be to decrease the content of sulfur in the UMC to counter the volume change. The reduced amount of sulfur in the composite would reduce the areal capacity, which could be recovered, however, by increasing the thickness of the electrode.

Figure 5 shows the discharge voltage profiles of the UMC−S composite cathode in an ether-based electrolyte (free of $LiNO_3$ additive). It should be emphasized that the reaction mechanism of the UMC−S electrode with lithium in ether-based electrolytes is slightly different. The linear ether molecules have better access to the sulfur in UMC compared to the cyclic carbonate molecules. Hence, the sulfur accessible to solvent molecules[38] will react similar to the sulfur confined in the mesoporous carbon.[1] Sulfur that is not reachable to solvent molecules will follow the quasi-solid-state reaction. In the first few cycles, the UMC−S composite features three voltage plateaus during discharge with ether-based electrolyte, in accordance with an earlier report.[39] The first two plateaus are due to the reduction of sulfur to higher-order polysulfides (Li_2S_x, x = 8−4) at 2.4−2.3 V and further to lower-order polysulfides (Li_2S_2/Li_2S) at 2.0−2.1 V. The third plateau at lower potential is assigned to the reduction of sulfur confined in ultramicropores, suggesting a solid-to-solid phase transition. From the sixth cycle, the discharge pattern constitutes only a quasi-solid-state behavior, as observed in the case of carbonate-based electrolyte. During the initial five cycles, the polysulfide might have dissolved in ether molecules and reacted at the

DOI: 10.1021/acsomega.8b01681
ACS Omega 2018, 3, 11290−11299

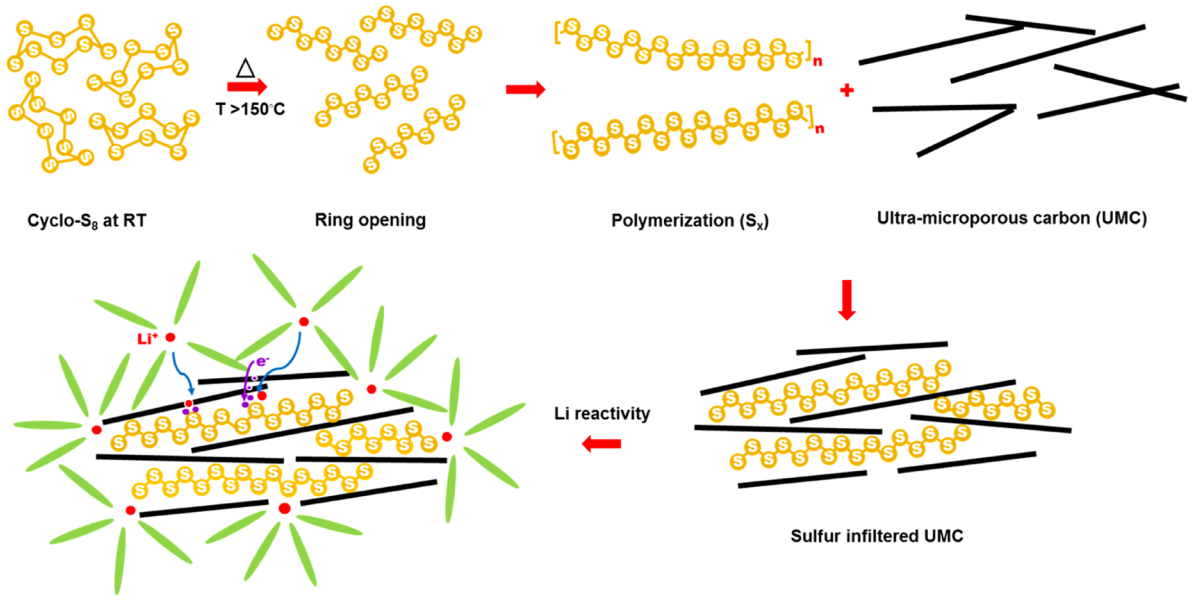

Figure 3. Schematic illustration of the preparation of UMC−S composites under vacuum.

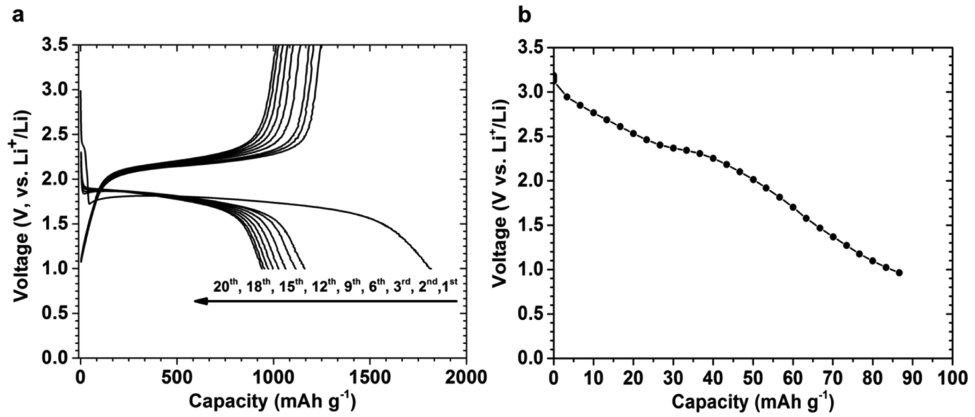

Figure 4. (a) Discharge/charge voltage profiles of UMC−S composite with carbonate electrolyte (1.0 M $LiPF_6$ in EC/DMC (1:1 v/v)) in the voltage range of 3.5−1 V at C/20. (b) Lithium insertion into the as-synthesized UMC host (first discharge).

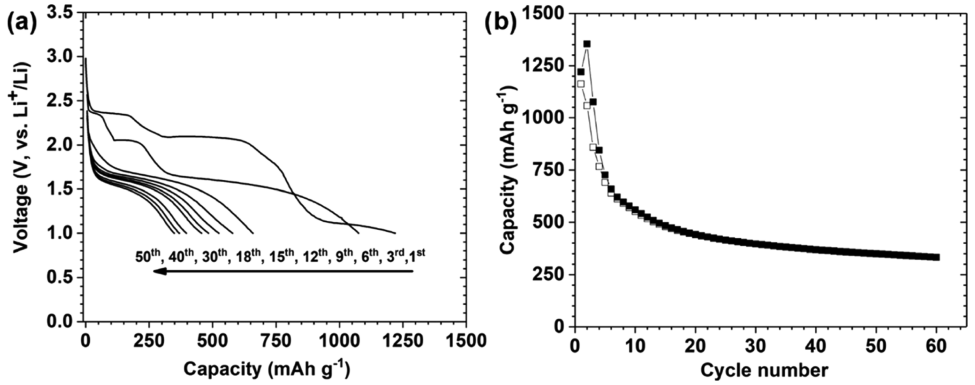

Figure 5. (a) Discharge/charge voltage profiles of UMC−S composite in the voltage range of 3.5−1 V at C/20 with ether-based electrolyte (1.0 M LiTFSI in dioxolane (DOL)/dimethoxyethane (DME) (1:1 v/v)) and (b) cycling behavior of the corresponding cell at C/20.

anode similar to that of sulfur confined in mesoporous carbon.[38,1]

A single voltage plateau is attained in discharge and charge profiles (Figures 4a and 5a), although the cells were operated between 3.5 and 1 V (after five cycles in ether-based electrolytes), which is above the solid electrolyte interphase (SEI) formation potential and irrespective of the electrolytes used. This underlines the importance of the carbon structure. Thus, without the necessity for a stable SEI, the size constraints in the UMC host reduced the contact between sulfur and solvent, thereby leading to quasi-solid-state behavior.

DOI: 10.1021/acsomega.8b01681
ACS Omega 2018, 3, 11290−11299

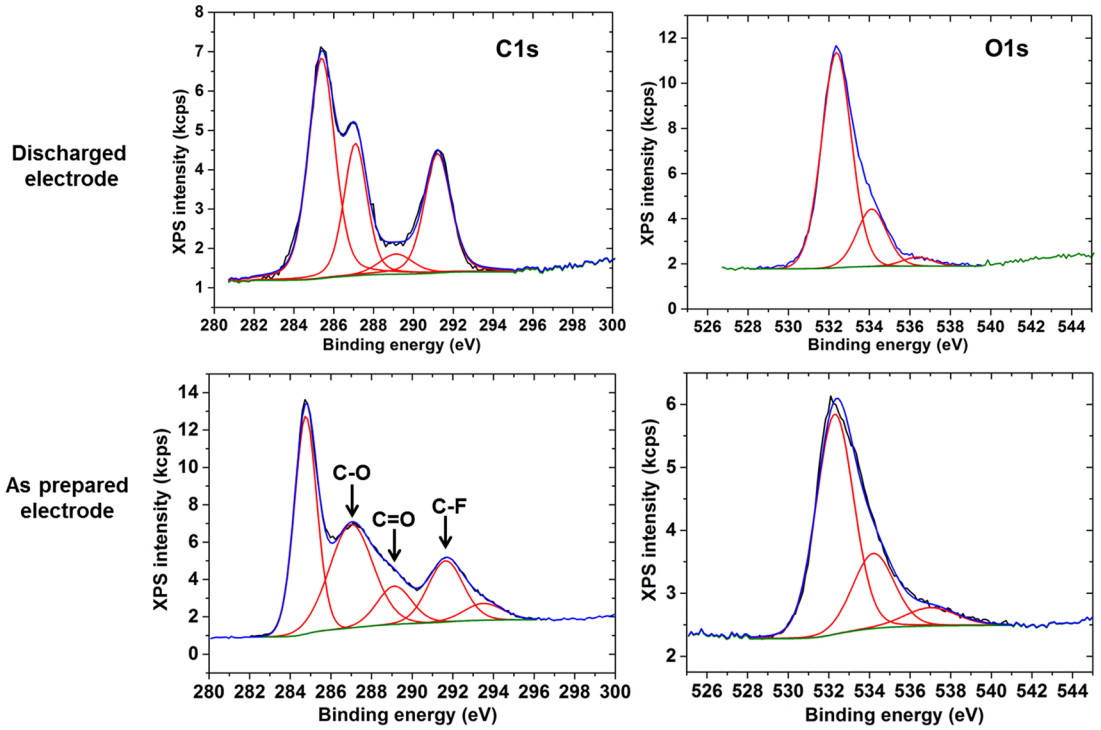

Figure 6. Comparison of XPS spectra in the C 1s and O 1s region for the as-prepared UMC−S electrode and after discharge to 1.0 V.

X-ray Photoelectron Spectroscopy (XPS) Analysis. Figure 6 compares the XPS spectra in the C 1s and O 1s region recorded on a UMC−S as-prepared electrode and after the first discharge. The C 1s XPS spectra of the as-prepared electrode exhibited three peaks at binding energies (BEs) of 287.0, 289.0, and 291.0 eV corresponding to C−O, C═O, and C−F bonds. During discharge, the peak at 289.0 eV, corresponding to C═O species, lost intensity considerably and almost disappeared due to the reaction with lithium. Consequently, the peak at 287.0 eV, corresponding to C−O, gained intensity after discharge. The peak at 291.0 eV, which corresponds to C−F bonds, is due to the binder poly(vinylidene difluoride) (PVDF). Considering the various plausible SEI components, an increase of the intensity of the peaks related to both C═O and C−O would be expected upon the growth of an SEI layer.[40] Instead, a decrease in C═O intensity is observed upon discharge from 3.5 to 1 V, which can be attributed to the reduction of the corresponding functional groups at the surface of the carbon host by lithium.[41] Therefore, SEI formation was not initiated at this point. This is in line with previous reports that, in the absence of additives in the carbonate-based or ether-based electrolyte, SEI formation is expected to occur only below 0.9 V (vs Li^+/Li).[40]

***In Situ* Raman Spectrum Analysis.** To probe the role of carbon (UMC) in transporting lithium to sulfur (as sulfur infused in UMC is isolated from the electrolyte molecules), *in situ* Raman spectroscopy measurements were performed on a UMC−S cathode at C/20. Here, we used 1.0 M $LiPF_6$ in EC/DMC (1:1 v/v) as electrolyte and an ECC-Opto-Std (EL-CELL GmbH) electrochemical cell. The voltage range was 1−3.5 V (vs Li^+/Li). Figure 7 shows the first discharge profile, and the inset shows the evolution of the D and G bands corresponding to the host UMC during discharge. The lithiation of the carbon−sulfur composite was expected to affect the Raman D-band (disordered or defective structures)

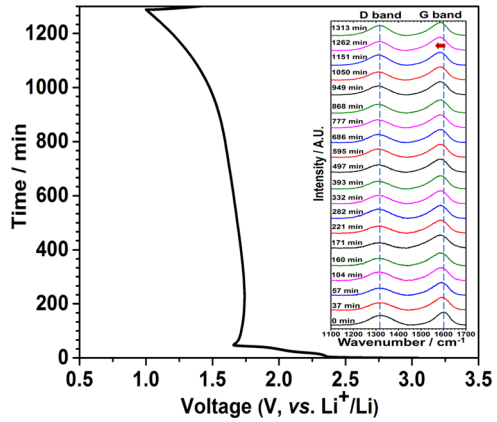

Figure 7. Discharge profile of UMC−S composite cathode vs Li at C/20 rate. The inset shows the *in situ* Raman spectra recorded during the discharge process.

and G-band (graphitic structures) of the carbon host.[42] During discharge, there was no weakening or broadening of the D-band. However, the position of the G-band was shifted to slightly lower wavenumbers during the initial discharge and remained unchanged until full discharge. Initially, carbon experienced a charge transfer, resulting in the reduction of the surface functional groups, which led to a red shift of the G-band.[43−47] From the *in situ* Raman spectroscopy measurements, we conclude that there is no insertion of Li into the carbon (UMC) host in the potential range of 1−3.5 V vs Li^+/Li and that the role of UMC is similar to that of a carbon-coated cathode material for Li-ion batteries.[48]

***In Situ* Electrochemical Impedance Spectroscopy (EIS).** To get further insight into the reactivity of UMC−S with lithium, *in situ* electrochemical impedance spectroscopy (EIS) measurements were performed on a UMC−S/Li cell during the first cycle. Impedance spectra were recorded at

DOI: 10.1021/acsomega.8b01681
ACS Omega 2018, 3, 11290−11299

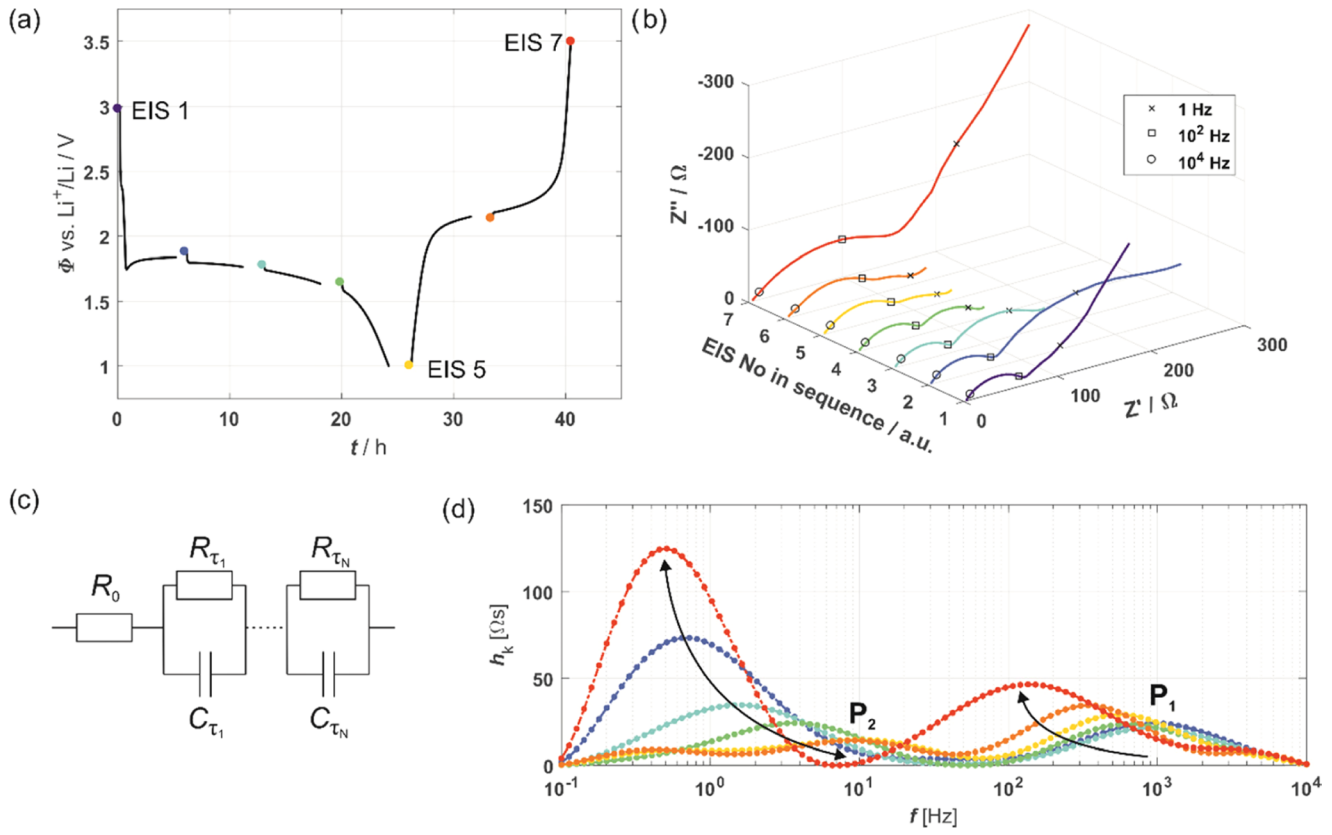

Figure 8. (a) Voltage profile of the cell discharged and charged to various states (at C/20) indicated as EIS1−EIS7; (b) impedance plots of the cell at various discharged and charged states (as denoted in (a)); (c) equivalent circuit; and (d) the distribution of relaxation time plot of the preprocessed impedance spectra.

various points of discharge and charge, as depicted in Figure 8a (EIS1−EIS7). Initially, impedance spectra were recorded at the open-circuit voltage potential (EIS1). Subsequently, the electrode was galvanostatically discharged for 5 h at a C/20 rate, followed by 1 h of equilibration. Then, the next impedance spectrum was recorded (EIS2). All other impedance spectra were recorded similarly in the frequency range of 200 kHz to 1 mHz, with a voltage amplitude of 5 mV. During post-processing (not shown here), it turned out that the as-recorded impedance spectra suffered from significant noise at frequencies below 0.1 Hz. Thus, the recorded spectra were cut at this frequency. From the Nyquist plot of the preprocessed data (Figure 8b), it is evident that the cell impedance was highest at EIS1. We attribute this high initial impedance to interfacial resistance. After discharging the sample for 5 h, the interfacial resistance was considerably reduced. The significant reduction of the interfacial resistance points toward less resistive products at the surface. Further discharging of the cell gradually reduced the impedance to a minimum at point EIS5, followed by an increase during subsequent charging (EIS7). The gradual decrease and increase of the impedance during the discharge and charge processes, respectively, indicate that the discharge products are less resistive than the charge products.

We have also analyzed the distribution of relaxation times for the measured impedance spectra. This method is well known for the identification of polarization losses in fuel cells[49,50] and batteries[51] and allows the deconvolution of the losses hidden in the impedance spectrum. Each point in the obtained distribution function represents the fraction of the polarization at a certain characteristic frequency and thus equals the resistance of a single resistor−capacitor circuit with the time constant τ_k in the measurement model shown in Figure 8c. The distribution functions of the preprocessed impedance spectra are shown in Figure 8d. Apparently, there are two processes, P_1 and P_2 (represented by two peaks in the distribution), which dominate the impedance response in the measured frequency range. Interestingly, these two processes follow different trends in the course of the first cycle: for P_1, constant expansion and shift to lower frequencies of the associated peak is observed, whereas both the shift and the dimension of the peak belonging to P_2 seem to be reversible with discharge and charge of the UMC−S electrode. For insertion materials, the frequency ranges observed for P_1 and P_2 (10 Hz to 1 kHz and 1−10 Hz, respectively) have already been identified in the literature and are commonly ascribed to losses from contact resistances (interparticle or at the particle−current collector interface) and faradic resistances associated with the charge-transfer reaction at the electrode−electrolyte interface, respectively.[51] In this context, the observed reversible dependency of P_2 on the open-circuit potential fits perfectly to the assignment mentioned above because the charge-transfer resistance is well known to depend on the lithiation degree of the insertion compound. The steady increase of the peak associated with process P_1 points toward a steady increase of the contact resistance, which might be caused by volume changes of the sulfur compound during the discharge and charge processes.

Overall Electrochemical Reaction Mechanism of Lithium with UMC−S Composite. In general, the reaction

DOI: 10.1021/acsomega.8b01681
ACS Omega 2018, 3, 11290−11299

of lithium with a carbon−sulfur composite cathode in a Li−S cell using different electrolytes can follow two types of reaction mechanisms, namely, a solid−liquid−solid reaction and/or a quasi-solid-state reaction. Electrochemically, these are reflected by two different types of voltage profiles. This difference in reaction mechanism is mainly due to the difference in the accessibility of solvent to the active component sulfur. If the solvent molecules are accessible to sulfur, then the reaction follows a solid−liquid−solid reaction mechanism; if the solvent access to sulfur is restricted, then the reaction follows a quasi-solid-state reaction mechanism. The former mechanism has been identified in mesoporous carbon (<2 nm) or microporous carbon (>0.7 nm) sulfur composites. However, the quasi-solid-state reaction mechanism is followed even in microporous carbon, provided it is pretreated by cycling at lower potentials to form a stable SEI.[32]

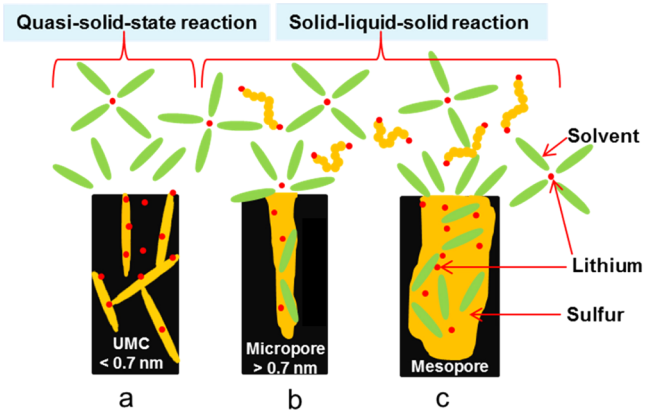

Figure 9. Schematic illustration of carbon−sulfur composites with carbon pores of varying size: (a) ultramicropore, (b) micropore, and (c) mesopores, and the related reactivity toward lithium in Li−S batteries.

Figure 9 illustrates the difference in solvent accessibility by sulfur in carbon pores of varying size (UMC, microporous and mesoporous carbon) in carbon−sulfur composites.

(i) In the case of ultramicropores (<0.7 nm in Figure 9a), solvated ions tend to be desolvated at the surface when the size of the pore is smaller than the size of the solvated ions.[7] Thus, ultramicropores can mitigate or prevent the dissolution of active material, as the solvent concentration is very low or nearly zero inside the pore. This results in a quasi-solid-state reaction mechanism, irrespective of the electrolyte used (carbonate- or ether-based).[39,52,53]

(ii) In the case of microporous (0.7 to ≤2 nm) carbon−sulfur composites, the solvated ions can still have access to the active material (Figure 9b).

(iii) In the case of mesoporous carbon−sulfur composites, the sulfur is even more accessible by the solvent molecules (Figure 9c), leading to the dissolution of active material and intermediate polysulfides. This results in two discharge plateaus in the ether-based electrolyte, while the cells were not cyclable in carbonate-based electrolytes.[21]

Origin of the Voltage Plateau. Several studies on sulfur confined in UMC displayed a single plateau during the discharge/charge process.[14,16,39,52−54] This is different from the two-plateau discharge and charge behavior of typical cyclo-S_8.[55,56] It was speculated that the smaller allotropes (S_2 to S_4) enable the direct formation of lower-order polysulfides, resulting in a single plateau in the discharge curve. Nevertheless, no evidence was reported to support the existence of smaller allotropes of sulfur in UMC. However, operando XAS on UMC−S electrodes suggests the gradual conversion of higher-order polysulfide (Li_2S_x) to lower-order polysulfides (Li_2S_2/Li_2S) during the electrochemical discharge.[36] In fact, for the first time, the higher-order and lower-order polysulfides were clearly differentiated. The observation of higher-order polysulfides during the initial stage of the discharge suggests that sulfur exists as linear polymeric sulfur rather than as smaller allotropes in the UMC host. Lower-order polysulfides are unlikely to combine and form higher-order polysulfides during discharge. This leads to the question of why a single plateau rather than two plateaus are found in the electrochemical discharge curve. The solid-state conversion potential of S_8 to Li_2S is 2.24 V vs Li^+/Li, considering the free energy change for the formation of Li_2S from S_8.[52] The conversion potential was calculated assuming cyclic S_8, and the potential may change depending on the sulfur polymorph.

$$1/8\ S_8 + 2Li^+ + 2e^- \leftrightarrow Li_2S,\ E^\circ = 2.24\ V$$

This suggests that the solid-state conversion of S_8 to Li_2S should result in a single plateau below 2.24 V. Smaller allotropes are not required for a single plateau. Indeed, the single plateau was also observed for solid-state Li−S batteries. Hence, the electrochemical reaction of lithium with sulfur infused in UMC could be considered as a solid-state conversion, where the electrolyte molecules have no direct access to the sulfur—a quasi-solid-state reaction. In the case of sulfur confined in mesoporous carbon, where sulfur is accessible to the electrolyte molecules,[38] the conversion of S_8 to Li_2S shows different thermodynamics (due to the dissolved sulfur or polysulfide), similar to iodine redox process, where the redox potential depends on the reaction medium.[57,58]

CONCLUSIONS

Among various sulfur hosts, UMC exhibits unique advantages toward the development of sustainable Li−S batteries, particularly in conventional carbonate-based electrolytes. The effective separation of solvent molecules and sulfur or polysulfide confined in ultramicropore reduces the side reactions between polysulfide and electrolyte. The elimination of polysulfide in the electrolyte also reduces the side reactions at the anode side. So far, it was postulated that sulfur confined in ultramicropores is present in the form of smaller sulfur allotropes, due to size constraints. However, our experimental results suggest that sulfur in UMC exists as linear polymeric sulfur rather than as smaller allotropes. We also showed that the electrochemical reactivity of lithium with sulfur confined in UMC is different from that of sulfur confined in microporous carbon, ultramicroporous carbon containing a significant amount of micropores, or mesoporous carbon. The size of the carbon pores plays a critical role in determining the reaction path of lithium with sulfur confined in it.

EXPERIMENTAL SECTION

Synthesis and Characterization of UMC and UMC−S Composite. Ultramicroporous carbon (UMC) was prepared

DOI: 10.1021/acsomega.8b01681
ACS Omega 2018, 3, 11290−11299

by KOH activation of the carbon derived from coconut shells. The coconut shell powder was carbonized at 600 °C for 2 h under Ar gas flow. The carbon obtained was mixed with KOH at a ratio of 1:4 (wt %) and activated under Ar flow. Initially, the mixture was heated to 400 °C and maintained at that temperature for 1 h, and then the temperature was raised to 800 °C and kept for 2 h. The activated carbon obtained was neutralized using dil. HCl and washed with water and dried. N_2 adsorption−desorption isotherms were obtained using a Micromeritics ASAP 2020 analyzer. The specific surface area was calculated using the Brunauer−Emmett−Teller (BET) method, and the pore-size distributions were calculated by the density functional theory (DFT) method. X-ray photoelectron spectroscopy (XPS) measurements were carried out with a PHI 5800 MultiTechnique ESCA System using Al Kα (1486.6 eV) monochromatized radiation. The measurements were done at a detection angle of 45°, using pass energies of 93.9 and 29.35 eV for survey and detail spectra, respectively. For binding energy calibration, the main C (1s) peak was set to 284.8 eV. The sample surfaces were sputtered for 3 and 10 min (5 kV; 1 μA; sputter rate, ∼1 nm min^{-1}) for subsurface analysis. Raman spectra were collected at RT using a confocal Raman microscope (InVia, Renishaw) in the spectral range 100−2500 cm^{-1}, using a He−Ne laser with a wavelength of 632.8 nm as the excitation source. TEM and EELS spectra were obtained using a Cs-corrected FEI Titan 80-300 microscope equipped with a GIF Quantum 965 energy filter and operated at 80 kV to avoid knock-on damage and to increase the energy resolution.

Electrochemical Measurements. The UMC−S composite (45.8 wt % of S) and PVDF binder were mixed in a weight ratio of 90:10 using *N*-methyl-2-pyrrolidinone as a solvent. The slurry obtained was coated on a stainless steel foil and dried at 90 °C overnight. The fabricated electrode contained around 2 mg cm^{-2} of sulfur loading. Li foil (Aldrich, 99.9%) was used as the anode. A borosilicate glass fiber sheet was used as the separator. Either 1 M $LiPF_6$ in 1:1 ethylene carbonate (EC)/dimethyl carbonate (DMC) mixture (LP30, BASF) or 1.0 M LiTFSI in dioxolane (DOL)/dimethoxyethane (DME) (1:1 v/v) mixture was used as the electrolyte. The cell assembly and electrode fabrication were done in an Ar-filled glovebox. Electrochemical studies were performed at RT using Swagelok type cells. The cells were cycled between 1.0 and 3.5 V vs Li^+/Li at different current densities using an Arbin battery cycling unit BT2000. For EIS measurements, an electrochemical workstation (Bio-Logic) was used. The amplitude was set at 5 mV in the frequency range of 200 kHz to 1 mHz.

***In Situ* Raman Studies.** *In situ* Raman measurements on UMC−S electrodes were performed using an ECC-Opto-Std (EL-CELL GmbH) electrochemical cell. A thick slurry containing UMC−S and PVDF in the ratio of 90:10 was deposited onto an stainless steel current collector (16 mm) with a 1 mm hole in the middle. The electrodes were dried in an oven at 90 °C for 12 h. The *in situ* cell was assembled using the UMC−S-coated current collectors as a positive electrode, lithium foil as an anode, and a borosilicate glass fiber soaked with 1 M $LiPF_6$ in 1:1 ethylene carbonate (EC)/dimethyl carbonate (DMC) (LP30, BASF) as separator and electrolyte. The assembled cell was connected to an IM6 electrochemical system (ZAHNER-Elektrik GmbH) for galvanostatic cycling. The *in situ* Raman cell was discharged and charged between 1.0 and 3.5 V vs Li^+/Li at a rate of C/20. Raman spectra were collected at RT using a confocal Raman microscope (InVia, Renishaw) in the spectral range of 1000−2500 cm^{-1} using a He−Ne laser with a wavelength of 632.8 nm. The laser power was set to ≈1.0 mW, and the spectrum acquisition time was 20 s.

AUTHOR INFORMATION

Corresponding Authors

*E-mail: helen.joseph@kit.edu (H.M.J.).
*E-mail: munnangi.reddy@kit.edu (M.A.R.).

ORCID

R. Jürgen Behm: 0000-0002-7565-0628
M. Anji Reddy: 0000-0001-9101-0252

Notes

The authors declare no competing financial interest.

ACKNOWLEDGMENTS

The authors thank Dr. Xiu-Mei Lin for assistance in the Raman spectroscopy measurements.

REFERENCES

(1) Ji, X.; Nazar, L. F. Advances in Li-S batteries. *J. Mater. Chem.* **2010**, *20*, 9821−9826.
(2) Ji, X.; Lee, K. T.; Nazar, L. F. A highly ordered nanostructured carbon−sulfur cathode for lithium−sulfur batteries. *Nat. Mater.* **2009**, *8*, 500−506.
(3) Manthiram, A.; Fu, Y.; Su, Y. S. Challenges and Prospects of Lithium Sulfur Batteries. *Acc. Chem. Res.* **2013**, *46*, 1125−1134.
(4) Dean, J. A. *Lange's Handbook of Chemistry*, 3rd ed.; McGraw-Hill Professional: New York, 1985; p 3.
(5) Yang, Y.; Zheng, G. Y.; Misra, S.; Nelson, J.; Toney, M. F.; Gui, Y. High-Capacity Micrometer-Sized Li_2S Particles as Cathode Materials for Advanced Rechargeable Lithium-Ion Batteries. *J. Am. Chem. Soc.* **2012**, *134*, 15387−15394.
(6) Wang, D.-W.; Zeng, Q.; Zhou, G.; Yin, L.; Li, F.; Cheng, H.-M.; Gentle, I. R.; Lu, G. Q. M. Carbon−sulfur composites for Li−S batteries: status and prospects. *J. Mater. Chem. A* **2013**, *1*, 9382−9394.
(7) Mikhaylik, Y. V.; Akridge, J. R. Polysulfide shuttle study in the Li/S battery system. *J. Electrochem. Soc.* **2004**, *151*, A1969−A1976.
(8) Barchasz, C.; Molton, F.; Duboc, C.; Leprêtre, J.-C.; Patoux, S.; Alloin, F. Lithium/sulfur cell discharge mechanism: an original approach for intermediate species identification. *Anal. Chem.* **2012**, *84*, 3973−3980.
(9) Song, M.-K.; Cairns, E. J.; Zhang, Y. Lithium/sulfur batteries with high specific energy: old challenges and new opportunities. *Nanoscale* **2013**, *5*, 2186−2204.
(10) Guo, J.; Xu, Y.; Wang, C. Sulfur-Impregnated Disordered Carbon Nanotubes Cathode for Lithium−Sulfur Batteries. *Nano Lett.* **2011**, *11*, 4288−4294.
(11) Zheng, G.; Yang, Y.; Cha, J. J.; Hong, S. S.; Cui, Y. Hollow Carbon Nanofiber-Encapsulated Sulfur Cathodes for High Specific Capacity Rechargeable Lithium Batteries. *Nano Lett.* **2011**, *11*, 4462−4467.
(12) Wang, H.; Yang, Y.; Liang, Y.; Robinson, J. T.; Li, Y.; Jackson, A.; Cui, Y.; Dai, H. Graphene-wrapped sulfur particles as a rechargeable lithium-sulfur battery cathode material with high capacity and cycling stability. *Nano Lett.* **2011**, *11*, 2644−2647.
(13) Jayaprakash, N.; Shen, J.; Moganty, S. S.; Corona, A.; Archer, L. A. Porous Hollow Carbon@Sulfur Composites for High-Power Lithium−Sulfur Batteries. *Angew. Chem., Int. Ed.* **2011**, *50*, 5904−5908.
(14) Zhang, B.; Qin, X.; Li, G. R.; Gao, X. P. Enhancement of long stability of sulfur cathode by encapsulating sulfur into micropores of carbon spheres. *Energy Environ. Sci.* **2010**, *3*, 1531−1537.
(15) Schuster, J.; He, G.; Mandlmeier, B.; Yim, T.; Lee, K. T.; Bein, T.; Nazar, L. F. Spherical Ordered Mesoporous Carbon Nanoparticles

DOI: 10.1021/acsomega.8b01681
ACS Omega 2018, 3, 11290−11299

with High Porosity for Lithium−Sulfur Batteries. *Angew. Chem., Int. Ed.* **2012**, *51*, 3591−3595.
(16) Helen, M.; Anji Reddy, M.; Diemant, T.; Golla-Schindler, U.; Behm, R. J.; Kaiser, U.; Fichtner, M. Single step transformation of sulphur to Li_2S_2/Li_2S in Li-S batteries. *Sci. Rep.* **2015**, *5*, No. 12146.
(17) Wang, J.; Yang, J.; Wan, C.; Du, K.; Xie, J.; Xu, N. Sulfur composite cathode materials for rechargeable Lithium batteries. *Adv. Funct. Mater.* **2003**, *13*, 487−492.
(18) Seh, Z. W.; Li, W.; Cha, J. J.; Zheng, G.; Yang, Y.; McDowell, M. T.; Hsu, P. C.; Cui, Y. Sulphur-TiO_2 yolk-shell nanoarchitecture with internal void space for long-cycle lithium-sulphur batteries. *Nat. Commun.* **2013**, *4*, No. 1331.
(19) Ji, X.; Evers, S.; Black, R.; Nazar, L. F. Stabilizing lithium-sulphur cathodes using polysulphide reservoirs. *Nat. Commun.* **2011**, *2*, No. 325.
(20) Lodi-Marzano, F.; Leuthner, S.; Sommer, H.; Brezesinski, T.; Janek, J. High-Performance Lithium−Sulfur Batteries using Yolk−Shell Type Sulfur−Silica Nanocomposite Particles with Raspberry-Like Morphology. *Energy Technol.* **2015**, *3*, 830.
(21) Gao, J.; Lowe, M. A.; Kiya, Y.; Abruña, H. D. Effects of Liquid Electrolytes on the Charge−Discharge Performance of Rechargeable Lithium/Sulfur Batteries: Electrochemical and in-Situ X-ray Absorption Spectroscopic Studies. *J. Phys. Chem. C* **2011**, *115*, 25132−25137.
(22) Yuan, L. X.; Feng, J. K.; Ai, X. P.; Cao, Y. L.; Chen, S. L.; Yang, H. X. Improved dischargeability and reversibility of sulfur cathode in a novel ionic liquid electrolyte. *Electrochem. Commun.* **2006**, *8*, 610−614.
(23) Wang, J.; Chew, S. Y.; Zhao, Z. W.; Ashraf, S.; Wexler, D.; Chen, J.; Ng, S. H.; Chou, S. L.; Liu, H. K. Sulfur−mesoporous carbon composites in conjunction with a novel ionic liquid electrolyte for lithium rechargeable batteries. *Carbon* **2008**, *46*, 229−235.
(24) Hassoun, J.; Scrosati, B. Moving to a Solid-State Configuration: A Valid Approach to Making Lithium-Sulfur Batteries Viable for Practical Applications. *Adv. Mater.* **2010**, *22*, 5198−5201.
(25) Hayashi, A.; Ohtomo, T.; Mizuno, F.; Tadanaga, K.; Tatsumisago, M. All-solid-state Li/S batteries with highly conductive glass−ceramic electrolytes. *Electrochem. Commun.* **2003**, *5*, 701−705.
(26) Su, Y.-S.; Manthiram, A. Lithium Sulfur Batteries with a Microporous Carbon Paper as a Bifunctional Interlayer. *Nat. Commun.* **2012**, *3*, No. 1166.
(27) Zhou, G.; Pei, S.; Li, L.; Wang, D.-W.; Wang, S.; Huang, K.; Yin, L.-C.; Li, F.; Cheng, H.-M. A Graphene−Pure-Sulfur Sandwich Structure for Ultrafast, Long-Life Lithium−Sulfur Batteries. *Adv. Mater.* **2014**, *26*, 625−631.
(28) Lu, W.; Liu, M.; Miao, L.; Zhu, D.; Wang, X.; Duan, H.; Wang, Z.; Li, L.; Xu, Z.; Gan, L.; Chen, L. Nitrogen-containing Ultramicroporous Carbon Nanospheres for High Performance Supercapacitor Electrodes. *Electrochim. Acta* **2016**, *205*, 132−141.
(29) Liu, M.; Zhao, F.; Zhu, D.; Duan, H.; Lv, Y.; Li, L.; Gan, L. Ultramicroporous carbon nanoparticles derived from metal−organic framework nanoparticles for high-performance supercapacitors. *Mater. Chem. Phys.* **2018**, *211*, 234−241.
(30) Yang, C.-P.; Yin, Y.-X.; Guo, Y.-G.; Wan, L.-J. Electrochemical (De)Lithiation of 1D Sulfur Chains in Li−S Batteries: A Model System Study. *J. Am. Chem. Soc.* **2015**, *137*, 2215−2218.
(31) Fu, C.; Wong, B. M.; Bozhilov, K. N.; Guo, J. Solid state lithiation−delithiation of sulphur in sub-nano confinement: a new concept for designing lithium−sulphur batteries. *Chem. Sci.* **2016**, *7*, 1224−1232.
(32) Markevich, E.; Salitra, G.; Talyosef, Y.; Chesneau, F.; Aurbach, D. Review—On the Mechanism of Quasi-Solid-State Lithiation of Sulfur Encapsulated in Microporous Carbons: Is the Existence of Small Sulfur Molecules Necessary? *J. Electrochem. Soc.* **2017**, *164*, A6244−A6253.
(33) Ward, A. T. Raman spectroscopy of sulfur, sulfur-selenium, and sulfur-arsenic mixtures. *J. Phys. Chem.* **1968**, *72*, 4133−4139.
(34) Tuinstra, F.; Koenig, J. L. Raman spectrum of graphite. *J. Chem. Phys.* **1970**, *53*, 1126−1130.
(35) Meyer, B. Elemental Sulfur. *Chem. Rev.* **1976**, *76*, 367−388.
(36) Dominko, R.; Vizintin, A.; Aquilanti, G.; Stievano, L.; Helen, M. J.; Munnangi, A. R.; Fichtner, M.; Arcon, I. Polysulfides Formation in Different Electrolytes from the Perspective of X-ray Absorption Spectroscopy. *J. Electrochem. Soc.* **2018**, *165*, A5014−A5019.
(37) Fujimori, T.; Morelos-Gómez, A.; Zhu, Z.; Muramatsu, H.; Futamura, R.; Urita, K.; Terrones, M.; Hayashi, T.; Endo, M.; Hong, S. Y.; Choi, Y. C.; Tománek, D.; Kaneko, K. Conducting linear chains of sulphur inside carbon nanotubes. *Nat. Commun.* **2013**, *4*, No. 2162.
(38) Zhang, W.; Qiao, D.; Pan, J.; Cao, Y.; Yang, H.; Ai, X. A Li^+-conductive microporous carbon−sulfur composite for Li-S batteries. *Electrochim. Acta* **2013**, *87*, 497−502.
(39) Li, Z.; Yuan, L.; Yi, Z.; Sun, Y.; Liu, Y.; Jiang, Y.; Shen, Y.; Xin, Y.; Zhang, Z.; Huang, Y. Insight into the Electrode Mechanism in Lithium-Sulfur Batteries with Ordered Microporous Carbon Confined Sulphur as the Cathode. *Adv. Energy Mater.* **2014**, *4*, No. 1301473.
(40) An, S. J.; Li, J.; Daniel, C.; Mohanty, D.; Nagpure, S.; Wood, D. L., III The state of understanding of the lithium-ion-battery graphite solid electrolyte interphase (SEI) and its relationship to formation cycling. *Carbon* **2016**, *105*, 52−76.
(41) Kim, S.; Kim, K. C.; Lee, S. W.; Jang, S. S. Thermodynamic and redox properties of graphene oxides for lithium-ion battery applications: a first principles density functional theory modeling approach. *Phys. Chem. Chem. Phys.* **2016**, *18*, 20600−20606.
(42) Sole, C.; Drewett, N. E.; Hardwick, L. J. *In situ* Raman study of lithium-ion intercalation into microcrystalline graphite. *Faraday Discuss.* **2014**, *172*, 223−237.
(43) Chan, C. T.; Ho, K. M.; Kamitakahara, W. A. Zone-center phonon frequencies for graphite and graphite-intercalation compounds-charge-transfer and intercalate-coupling effects. *Phys. Rev. B* **1987**, *36*, 3499−3502.
(44) Kertesz, M. Changes of lattice geometries upon charge-transfer. *Mol. Cryst. Liq. Cryst.* **1985**, *126*, 103−110.
(45) Inaba, M.; Yoshida, H.; Ogumi, Z. *In situ* Raman study of electrochemical lithium insertion into mesocarbon microbeads heat-treated at various temperature. *J. Electrochem. Soc.* **1996**, *143*, 2572−2578.
(46) Wang, Z. X.; Huang, X. J.; Xue, R. J.; Chen, L. Q. A new possible mechanism of lithium insertion and extraction in low-temperature pyrolytic carbon electrode. *Carbon* **1999**, *37*, 685−692.
(47) Endo, M.; Kim, C.; Karaki, T.; Fujino, T.; Matthews, M. J.; Brown, S. D. M.; Dresselhaus, M. S. *In situ* Raman study of PPP-based disordered carbon as an anode in a Li ion battery. *Synth. Met.* **1998**, *98*, 17−24.
(48) Li, H.; Zhou, H. Enhancing the performances of Li-ion batteries by carbon-coating: present and future. *Chem. Commun.* **2012**, *48*, 1201−1217.
(49) Schichlein, H.; Müller, A. C.; Voigts, M.; Krügel, A.; Ivers-Tiffée, E. Deconvolution of electrochemical impedance spectra for the identification of electrode reaction mechanisms in solid oxide fuel cells. *J. Appl. Electrochem.* **2002**, *32*, 875−882.
(50) Weiß, A.; Schindler, S.; Galbiati, S.; Danzer, M. A.; Zeis, R. Distribution of Relaxation Times Analysis of High-Temperature PEM Fuel Cell Impedance Spectra. *Electrochim. Acta* **2017**, *230*, 391−398.
(51) Illig, J.; Ender, M.; Chrobak, T.; Schmidt, J. P.; Klotz, D.; Ivers-Tiffée, E. Separation of Charge Transfer and Contact Resistance in $LiFePO_4$-Cathodes by Impedance Modeling. *J. Electrochem. Soc.* **2012**, *159*, A952−A960.
(52) Xu, Y.; Wen, Y.; Zhu, Y.; Gaskell, K.; Cychosz, K. A.; Eichhorn, B.; Xu, K.; Wang, C. Confined Sulfur in Microporous Carbon Renders Superior Cycling Stability in Li/S Batteries. *Adv. Funct. Mater.* **2015**, *25*, 4312−4320.
(53) Takahashi, T.; Yamagata, M.; Ishikawa, M. A sulfur−microporous carbon composite positive electrode for lithium/sulfur and silicon/sulfur rechargeable batteries. *Prog. Nat. Sci.: Mater. Int.* **2015**, *25*, 612−621.
(54) Xin, S.; Gu, L.; Zhao, N.-H.; Yin, Y.-X.; Zhou, L.-J.; Guo, Y.-G.; Wan, L.-J. Smaller Sulfur Molecules Promise Better Lithium−Sulphur Batteries. *J. Am. Chem. Soc.* **2012**, *134*, 18510−18513.

DOI: 10.1021/acsomega.8b01681
ACS Omega 2018, 3, 11290−11299

(55) Manthiram, A.; Fu, Y.; Chung, S.-H.; Zu, C.; Su, Y.-S. Rechargeable Lithium−Sulfur Batteries. *Chem. Rev.* **2014**, *114*, 11751−11787.
(56) Adelhelm, P.; Hartmann, P.; Bender, C. L.; Busche, M.; Eufinger, C.; Janek, J. From lithium to sodium: cell chemistry of room temperature sodium−air and sodium−sulfur batteries. *Beilstein J. Nanotechnol.* **2015**, *6*, 1016−1055.
(57) Amatucci, G. G.; Pereira, N.; Badway, F.; Sina, M.; Cosandey, F.; Ruotolo, M.; Cao, C. Formation of lithium fluoride/metal nanocomposites for energy storage through solid state reduction of metal fluorides. *J. Fluorine Chem.* **2011**, *132*, 1086−1094.
(58) Tarascon, J. M.; Guyomard, D. Li Metal-free rechargeable batteries based on $Li_{1+x}Mn_2O_4$ cathodes ($0 \leq x \leq 1$) and carbon anodes. *J. Electrochem. Soc.* **1991**, *138*, 2864−2868.

DOI: 10.1021/acsomega.8b01681
ACS Omega 2018, 3, 11290−11299